Simulation for Polychromatic L-Shell X-ray Fluorescence Computed Tomography with Pinhole Collimator

Shanghai Jiang
Key Laboratory of Optoelectronics Technology and System, Ministry of Education, Chongqing University, Chongqing, China

Mianyi Chen
Department of Biomedical Engineering, Rensselaer Polytechnic Institute, Troy, NY, USA

Peng Feng
Key Laboratory of Optoelectronics Technology and System, Ministry of Education, Chongqing University, Chongqing, China
coe-fp@cqu.edu.cn;

Peng He
Key Laboratory of Optoelectronics Technology and System, Ministry of Education, Chongqing University, Chongqing, China

Luzhen Deng
Department of Radiation Physics, the University of Texas MD Anderson Cancer Center, Houston, TX 77030, USA

Biao Wei
Key Laboratory of Optoelectronics Technology and System, Ministry of Education, Chongqing University, Chongqing, China
weibiao@cqu.edu.cn;

***Abstract*—As a novel imaging method, X-ray fluorescence computed tomography (XFCT) has attracted wide concern in recent years. In this paper, a polychromatic L-shell XFCT with pinhole collimator was proposed to save scanning time and improve detection limit of imaging system. First, imaging theoretical formulas were derived. Then, two phantoms (A and B) filled with polymethyl methacrylate (PMMA) were imaged by Monte Carlo simulation. The phantom A is embedded with six GNP (gold nanoparticles)-loaded cylinders with same radius (1.5mm) and height (10mm) but different Au weight concentration ranging from 0.2% to 1.2%. The phantom B is embedded with eight GNP-loaded cylinders with same Au weight concentration (1%) and height (10mm) but different radius ranging from 0.1mm to 0.8mm. At last, the reconstructed XFCT images were reconstructed by maximum likelihood expectation maximization (MLEM) with un-correction and correction, respectively. In this study, the feasibility of the proposed imaging system was demonstrated by Monte Carlo simulation.**

Keywords—L-shell XFCT, Monte Carlo simulation, pinhole collimator.

I. INTRODUCTION

Because it can simultaneously obtain structural, functional and molecular information in a nondestructive and noninvasive method, X-ray Fluorescence Computed Tomography (XFCT) has attracted wide concern in recent years. When incident X-rays interact with imaging probes containing high atomic number (Z) elements, fluorescent X-rays will emit from samples, and measured with a photon-counting detector. The distribution and content of high-Z element can be reconstructed from projections, which are acquired by rotating X-ray source[1, 2].

Conventional imaging geometries were time-consuming process. Some novel imaging geometries, such as pinhole collimator, slit collimator and multiple-pinhole collimator, were proposed to solve the problem by some researchers[3]. However, few literatures mentioned these imaging methods can be applied in *L*-shell XFCT.

In this study, we propose a benchtop imaging system for polychromatic *L*-shell XFCT based on pinhole effect with sheet-beam geometry. Then, imaging theoretical formulas are derived. Two phantoms contained several GNP-loaded regions are imaged by Monte Carlo simulations. The XFCT images are reconstructed by MLEM with un-correction and correction, respectively. Contrast to noise ratio (CNR) are calculated to evaluate image quality, and CNR for the reconstructed images as functions of Au weight concentration and size of GNP-loaded regions are evaluated.

II. METHODS AND MATERIALS

A. Imaging system

The imaging system proposed in our study is shown in Fig.1. which consists of polychromatic X-ray source, pinhole collimator, fluorescent array detectors and CCD.

The X-rays emitted by tube source are collimated by a lead collimator into parallel sheet beam, then impinge on the phantom to cover the imaging cross-section. The phantom within high Z elements irradiated by X-ray beam can isotropically emit characteristic X-rays, which partially pass through the pinhole to linear array photon-counting detectors with energy resolution. The recorded data is transferred to computer for image reconstruction.

DOI: 10.12059/Fully3D.2017-11-3203008

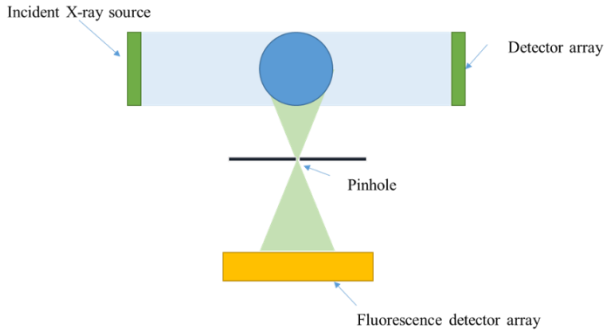

Fig.1. schematic diagram of XFCT imaging system based on pinhole collimator with sheet-beam

B. *Geometry model of XFCT based on pinhole*

The imaging geometry of sheet-beam XFCT with pinhole collimator is presented in Fig.2. Two coordinate systems, including *st*- coordinate system and *xy*-coordinate system, are established to describe the whole imaging process. Here, we assume that X-ray source and detection system are fixed to *st*-coordinate, while the phantom is fixed to *xy*-coordinate system[4]. The *st*-coordinate system is spun and can be at any instant obtained by rotating the *xy*-coordinate system by an angle θ counterclockwise. Their relationship can be expressed as follows:

$$\begin{pmatrix} s \\ t \end{pmatrix} = \begin{pmatrix} \cos\theta & \sin\theta \\ -\sin\theta & \cos\theta \end{pmatrix} \begin{pmatrix} x \\ y \end{pmatrix} \tag{1}$$

As shown in Fig.2, incident sheet-beam can be considered as independent X-rays and the incident X-ray intersects with line segment of the phantom between point *P* and point *Q*. We consider the point *R* on the line segment *PQ*, which emits X-ray fluorescent photons isotropically. The emitted X-rays pass through the pinhole to the detectors. The measurement process can be described as follows:

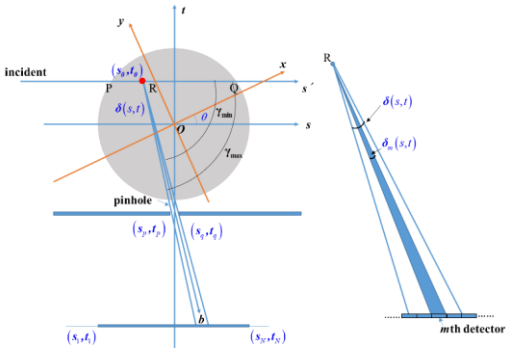

Fig.2. Schematic diagram of XFCT imaging geometry based on pinhole collimator

step1: The incident X-ray travels from *P* to *R* while being attenuated by the phantom. The flux at point *R* can be expressed as:

$$I_R(s,t) = I_0 \exp\left(-\int_{-\infty}^{s} \mu^I(s,t)\,ds\right) \tag{2}$$

Where I_0 is the flux of incident X-rays, and $\mu^I(s,t)$ is the linear attenuation coefficient of element at incident intensity.

Step2: The emitted X-rays at point *R*, which pass through pinhole, can be given by

$$\mu_{ph}\Delta s\omega I_0\delta(s,t)\exp\left(-\int_{-\infty}^{s}\mu^I(s,t)\,ds\right)\rho(s,t) \tag{3}$$

Where μ_{ph} the photoelectric linear coefficient of the element, ω is the field of fluorescent X-ray, and $\rho(s,t)$ is the element weight concentration. Δs and $\delta(s,t)$ are the differential of *s* and solid angle at which the point, *R*, viewed by the pinhole, respectively.

Step3: We number the fluorescent array detector with *m* ranging from 1 to *M*. Because the X-rays passing through pinhole may cover several fluorescent detectors, the angle δ should be divided into several parts according to the covered detectors. Considering the covered detector with number *m*, a single X-ray emitted from the point, *R*, reaching the *m*th detector, is attenuated along segment *RS*. Let $\mu^F(s,t)$ be the linear attenuation coefficient of fluorescent X-ray. The attenuation of X-ray fluorescence can be expressed as

$$\exp\left[-\int_0^{\infty}\mu^F(s-b\cos\gamma, s+b\sin\gamma)\,db\right] \tag{4}$$

The total attenuation of X-ray fluorescence emitted from point *R* is given by

$$\int_{\gamma_{\min}}^{\gamma_{\max}}\exp\left[-\int_0^{\infty}\mu^F(s-b\cos\gamma, s+b\sin\gamma)\,db\right]d\gamma \tag{5}$$

The total intensity of the fluorescent X-ray, emitted from the segment *PQ*, reaching the *m*th detector, can be calculated by

$$\begin{aligned} I' = {} & \mu_{ph}\omega I_0\int_{-\infty}^{+\infty}\delta_m(s,t)\exp\left[-\int_{-\infty}^{s}\mu^I(s',t)\,ds'\right]\rho(s,t) \\ & \cdot\int_{\gamma_{\min}}^{\gamma_{\max}}\exp\left[-\int_0^{\infty}\mu^F(s+b\cos\gamma, t-b\sin\gamma)\,db\right]d\gamma\,ds \end{aligned} \tag{6}$$

Where $\delta_m(s,t)$ is the angle at point, *R*, viewed by the *m*th detector. The intensity of total emitted X-ray fluorescence reaching the *m*th detector is obtained by integrating I' with respect to *t* from negative infinity to positive infinity, which can be given by

$$\begin{aligned} I_m(\theta) = {} & \mu_{ph}\omega I_0\int_{-\infty}^{+\infty}\int_{-\infty}^{+\infty}\delta_m(s,t)\exp\left[-\int_{-\infty}^{s}\mu^I(s',t)\,ds'\right]\rho(s,t) \\ & \cdot\int_{\gamma_{\min}}^{\gamma_{\max}}\exp\left[-\int_0^{\infty}\mu^F(s+b\cos\gamma, t-b\sin\gamma)\,db\right]d\gamma\,ds\,dt \\ = {} & \iint_D \delta_m(s,t)\,f(\theta,s,t)\,g(\theta,s,t)\,\rho(s,t)\,ds\,dt \end{aligned} \tag{7}$$

Here, integral region, *D*, is part of the whole image section, where the emitted fluorescent X-rays can reach the *m*th detector and

$$f(\theta,s,t) = I_0\exp\left[-\int_{-\infty}^{s}\mu^I(s',t)\,ds'\right] \tag{8}$$

$$g(\theta,s,t) = \mu_{ph}\omega\int_{\gamma_{\min}}^{\gamma_{\max}}\exp\left[-\int_0^{\infty}\mu^F(s+b\cos\gamma, t-b\sin\gamma)\,db\right]d\gamma \tag{9}$$

If the $\mu^I(s,t)$ and $\mu^F(s,t)$ are neglected in equation (7), it can be also expressed approximately as follows:

$$I_m(\theta) \approx \mu_{ph}\omega I_0\delta_m\iint_D \rho(s,t)\,ds\,dt \tag{10}$$

Maximum Likelihood Expectation Maximization (MLEM) algorithm was used to reconstruct XFCT images in this study. In order to evaluate the influence of absorption for incident X-rays and emitted fluorescent X-rays, the XFCT images were reconstructed with and without attenuation correction, respectively.

C. Monte Carlo simulation

In this study, the imaging process was simulated by MCNP software. The imaging process at each angle of projection can be considered as an independent simulation. For each independent simulation, the X-ray tube source need be simulated, which is repeated and time-consuming. We replace the simulation of X-ray tube with a virtual source to reduce the time of simulation, where its spectrum was calculated by SpekCal software[5]. The spectrum of sheet beam X-ray source was shown in Fig.3. The phantoms were scanned with 10mm width of sheet beam. The positions of pinhole and fluorescent array detectors were the same as in numerical simulation. The array detectors including 128 elements are energy-sensitive. Each element of array detectors can record all the fluorescent X-rays and Compton scattering X-rays from 6.5keV to 62keV at every 0.5keV. When 1×10^8 histories are used for each simulation, the uncertainty was less than 5% for relevant photon energies (8-13keV). To acquire fluorescent photons, cubic polynomial was used to fit the points eliminated *L*-shell fluorescent peaks. The fluorescent photons for each detector element was the difference between the measured photons and the fitted photons[6]. The sinogram was reconstructed using the fluorescent photons from all the simulations.

Two GNP-loaded PMMA phantoms in Fig.4 are imaged by Monte Carlo simulation. The phantoms are cylinders with same size, 10mm, in height and diameter. Six small cylinders with GNPs, which has the same size in diameter (1.5mm) and height (10mm) but different concentration ranging from 0.2% to 1.2%, are embedded in phantom *A*. In phantom *B*, eight cylinders with 1% GNPs but different diameters ranging from 0.2mm to 1.6mm are embedded. The radius of pinhole is 100μm. The distance from the pinhole to the center of phantom is 4.5 cm, and the distance from the pinhole to array detectors is also 4.5cm. The phantoms are scanned with a rotational step 3 °.

III. RESULTS

According to previous description, the sinograms of the two phantoms are reconstructed. Here, Fig.5(a) is the sinogram of phantom A and Fig.5(b) is the sinogram of phantom B. The reconstructed images by MLEM algorithm are shown in Fig.6. The gray values in Fig.6(a) show an increase with the increase of Au weight concentration. The corrected images also have higher contrast and sharper edges than the uncorrected ones. Affected by self-absorption, the concentration distribution of GNPs-loaded regions in Fig.6(a) and Fig.6(c) is also not uniform. In the corrected images (Fig.6(b)and Fig.6(d)), the uniformity of concentration distribution has been partly optimized.

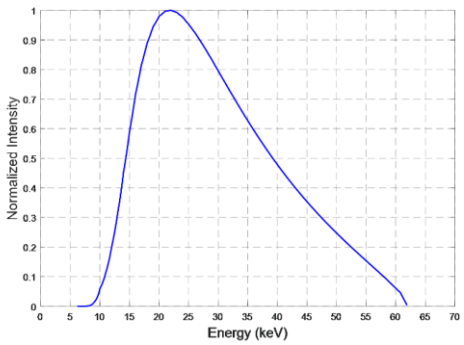

Fig.3. Spectrum of incident X-ray tube source.

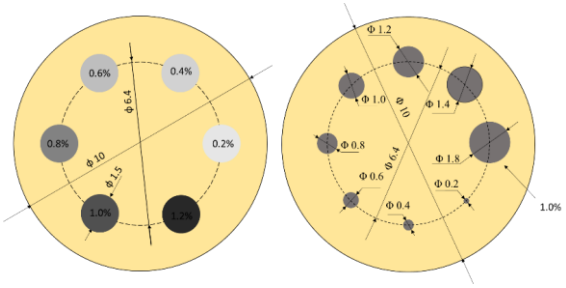

Fig.4. Phantoms contained GNP-loaded region. (a) GNP-loaded region with same radius but different Au weight concentration. (b) GNP-loaded regions with different radius but same Au weight concentration.

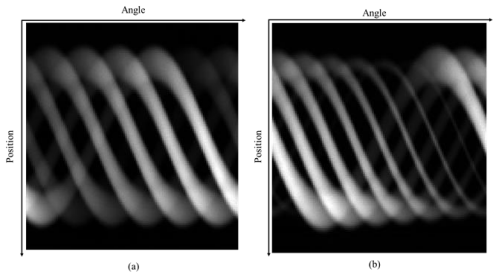

Fig.5. The reconstructed sinograms acquired by Monte Carlo simulation. (a) is the sinogram of phantom *A* and (b) is the sinogram of phantom *B*.

The reconstructed XFCT images were evaluated as CNR by calculating the ratio of difference between the mean value of each GNP-loaded region and background (PMMA) and standard deviation of background. CNR is expressed as follows[7]:

$$CNR = \frac{\bar{\Psi}_{\text{Region}} - \bar{\Psi}_{BK}}{V_{BK}} \tag{11}$$

Where $\bar{\Psi}_{\text{Region}}$ and $\bar{\Psi}_{BK}$ are mean reconstructed values of GNP-loaded region and background, V_{BK} is standard deviation of background (PMMA). According to the Rose criterion, imaging sensitivity limit of the system proposed was determined using CNR of 4.

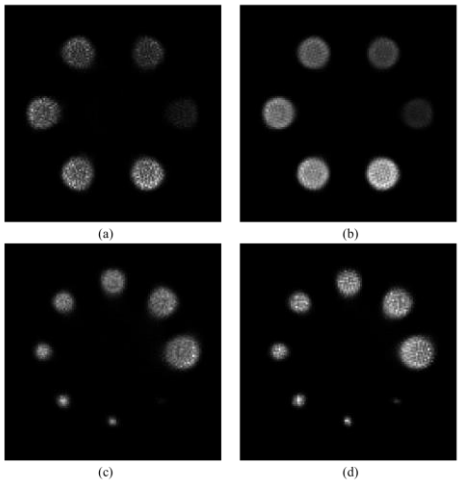

Fig.6 Reconstruction images of phantoms in Monte Carlo simulation. (a) and (c) reconstructed by MLEM without correction, (b) and (d) reconstructed by MLEM with correction.

In Fig.7 and Fig.8, CNR for the corrected images are higher than the uncorrected ones, and all the CNR values are greater than 4, which means all GNPs-loaded regions are detectable according Rose criterion. Fig.7 indicates that CNR of GNPs-loaded region for the same size is linear proportional to Au weight concentration (R^2=0.98).

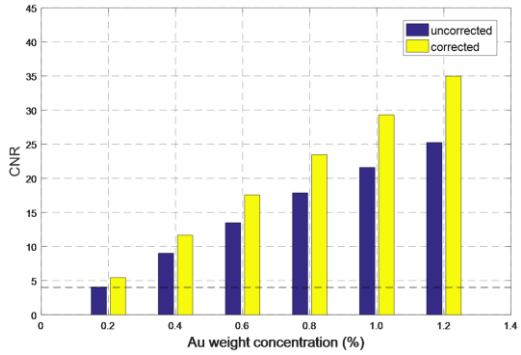

Fig.7. CNRs for reconstructed XFCT images by MLEM as a function of Au weight concentration.

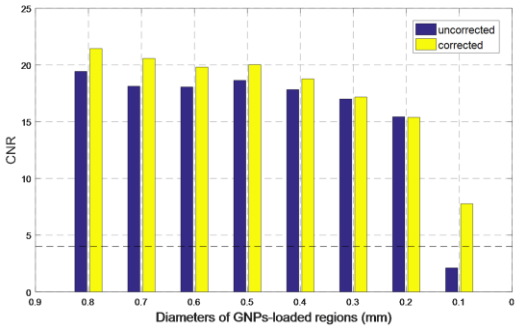

Fig.8. CNRs for reconstructed XFCT image by MLEM as a function of GNP-loaded region size

CNR for the corrected images has the decreasing trend with radius of GNPs-loaded region ranging from 0.8mm to 0.1mm in Fig.8, especially for the smallest region, a sharp decrease of CNR will significantly influence the detectability.

IV. CONCLUSION

In this investigation, the feasibility of polychromatic sheet-beam XFCT based on pinhole collimator was demonstrated Monte Carlo simulations. XFCT images were reconstructed by MLEM algorithm with and without correction, respectively. Attenuation can be corrected by the proposed method, and contrast to noise ratio (CNR) is linear proportional to Au weight concentration. Although only 2D image reconstruction was discussed in this paper, 3D images can be obtained by stacking.

ACKNOWLEDGMENT

This work is partially supported by the National Natural Science Foundation of China (61201346, 61401049), the Graduate Scientific Research and Innovation Foundation of Chongqing, China (Grant no. CYB16044), Chongqing strategic industry key generic technology innovation project (NO. cstc2015zdcy-ztzxX0002).

REFERENCES

[1]. B. Laforce, B. Vermeulen, J. Garrevoet, B. Vekemans, L. V. Hoorebeke, C. Janssen, and L. Vincze, “Laboratory Scale X-ray Fluorescence Tomography: Instrument Characterization and Application in Earth and Environmental Science,” *Analytical Chemistry*, vol. 88, no. 6, pp. 3386-91, 2016.

[2]. Q. Yang, B. Deng, G. Du, H. Xie, G. Zhou, T. Xiao, and H. Xu, “X-ray fluorescence computed tomography with absorption correction for biomedical samples,” *X-Ray Spectrometry*, vol. 43, no. 5, pp. 278-285, 2014.

[3]. T. Sasaya, D. Aoki, T. Yuasa, K. Hyodo, N. Sunaguchi, and T. Zeniya, "EM-TV reconstruction algorithm for pinhole-type fluorescent X-ray computed tomography." 10th Asian Control Conference, 31 May, pp. 1-6. 2015

[4]. P. Feng, W. Cong, B. Wei, and G. Wang, “Analytic Comparison between X-ray Fluorescence CT and K-edge CT,” *IEEE Transactions on Biomedical Engineering*, vol. 61, no. 3, pp. 975-985, 2014.

[5]. G. Poludniowski, G. Landry, F. DeBlois, P. M. Evans, and F. Verhaegen, “SpekCalc: a program to calculate photon spectra from tungsten anode x-ray tubes,” *Physics in Medicine and Biology*, vol. 54, no. 19, pp. N433-8, 2009.

[6]. B. L. Jones, and S. H. Cho, “The feasibility of polychromatic cone-beam x-ray fluorescence computed tomography (XFCT) imaging of gold nanoparticle-loaded objects: a Monte Carlo study,” *Physics in Medicine and Biology*, vol. 56, no. 12, pp. 3719-30, 2011.

[7]. M. Bazalova-Carter, M. Ahmad, T. Matsuura, S. Takao, Y. Matsuo, R. Fahrig, H. Shirato, K. Umegaki, and L. Xing, “Proton-induced x-ray fluorescence CT imaging,” *Medical Physics*, vol. 42, no. 2, pp. 900-7, 2015.